Chemical Science

ROYAL SOCIETY OF CHEMISTRY

PERSPECTIVE

View Article Online
View Journal | View Issue



Cite this: *Chem. Sci.*, 2021, **12**, 4201

All publication charges for this article have been paid for by the Royal Society of Chemistry



# The atomic-level regulation of single-atom site catalysts for the electrochemical $CO_2$ reduction reaction

Qingyun Qu, Shufang Ji, Yuanjun Chen,* Dingsheng Wang * and Yadong Li

The electrochemical $CO_2$ reduction reaction ($CO_2$RR) is viewed as a promising way to remove the greenhouse gas $CO_2$ from the atmosphere and convert it into useful industrial products such as methane, methanol, formate, ethanol, and so forth. Single-atom site catalysts (SACs) featuring maximum theoretical atom utilization and a unique electronic structure and coordination environment have emerged as promising candidates for use in the $CO_2$RR. The electronic properties and atomic structures of the central metal sites in SACs will be changed significantly once the types or coordination environments of the central metal sites are altered, which appears to provide new routes for engineering SACs for $CO_2$ electrocatalysis. Therefore, it is of great importance to discuss the structural regulation of SACs at the atomic level and their influence on $CO_2$RR activity and selectivity. Despite substantial efforts being made to fabricate various SACs, the principles of regulating the intrinsic electrocatalytic performances of the single-atom sites still needs to be sufficiently emphasized. In this perspective article, we present the latest progress relating to the synthesis and catalytic performance of SACs for the electrochemical $CO_2$RR. We summarize the atomic-level regulation of SACs for the electrochemical $CO_2$RR from five aspects: the regulation of the central metal atoms, the coordination environments, the interface of single metal complex sites, multi-atom active sites, and other ingenious strategies to improve the performance of SACs. We highlight synthesis strategies and structural design approaches for SACs with unique geometric structures and discuss how the structure affects the catalytic properties.

Received 27th December 2020
Accepted 17th February 2021

DOI: 10.1039/d0sc07040h

rsc.li/chemical-science

## 1. Introduction

The scalable applications of fossil fuels have generated huge technological developments and resulted in significant improvements in people's living conditions. However, it also causes a high concentration of $CO_2$ in the atmosphere, which contributes to the aggravation of the greenhouse effect, thus shifting ecological balance and accelerating ice sheet melting in Eastern Antarctica.[1] There is a general agreement that efforts should be made to control and reduce the $CO_2$ concentration in the atmosphere. Although fossil fuel is a significant part of our

*Department of Chemistry, Tsinghua University, Beijing 100084, China. E-mail: chenyuan15@mails.tsinghua.edu.cn; wangdingsheng@mail.tsinghua.edu.cn*

*Qingyun Qu is currently a senior student at Tsinghua University, majoring in Chemistry. Her current research interests are the rational design and synthesis of single-atom site catalysts and their application in electrocatalysis.*

*Shufang Ji received her B.S. (2011), M.S. (2014), and Ph.D. (2018) degrees in chemistry from Qufu Normal University, Soochow University, and Tsinghua University, respectively. She is currently working in Prof. Yadong Li's group as a postdoctoral fellow in the Department of Chemistry at Tsinghua University. Her research interests involve the synthesis and applications of well-defined single-atom site catalysts and supported cluster catalysts.*

energy structure, $CO_2$ emission is inevitable. Capturing, storing and converting $CO_2$ has become a promising way to remove $CO_2$ from the atmosphere.[2] Significant efforts have been made in this field, the $CO_2$ reduction reaction ($CO_2RR$) has become one of the hottest topics among them.[3] The products of the $CO_2RR$ are mainly methane, methanol, formate, ethanol, and so on, which are widely used in industrial production. The valuable products of $CO_2RR$ have attracted extensive attention in this field in recent years. There are various approaches used to achieve $CO_2$ reduction, compared to thermocatalysis, biocatalysis and photocatalysis, electrocatalysis has more moderate reaction conditions, lower costs and higher yields.[4–10] The electrochemical reduction of $CO_2$ can use electricity generated from renewable energy, such as wind energy and hydro-energy.[11] The conversion from electrical energy to the chemical energy of $CO_2RR$ products can be viewed as a storage form of renewable energy, which is safe and convenient for transportation and long-term storage.

However, there still remains great challenges for the $CO_2RR$, as it has sluggish kinetics, a complex multi-electron mechanism and a hydrogen evolution reaction (HER) competition reaction.[12,13] The $CO_2RR$ performance of catalysts is related to the rate determining steps, including $CO_2$ adsorption, *COOH and *CO formation on the active sites, which is decided by the adsorption free energy of $CO_2$, the binding energy of the intermediates, the electron transfer rate and so on.[14,15] For further reactions, the binding energy of intermediates, especially *CO is also crucial to the formation of $C_2^+$ products. Therefore, it is of great importance to manipulate the electronic and geometric structure of the catalysts, which can regulate the rate determining steps by changing the binding and formation energies of the intermediates, thus changing the activity and selectivity of the $CO_2RR$.[16,17]

Among all the kinds of catalysts used, single-atom site catalysts (SACs) have drawn significant attention owing to their unique structure and properties, which have great potential to bridge the gap between homogenous and heterogeneous catalysts.[18–22] SACs feature isolated metal atoms dispersed on substrates as active sites, which result in multiple advantages: (i) they have the maximum theoretical atom utilization.[23–25] (ii) Single metal atoms, as active centers, generate low-coordination environments, as well as unique electronic and geometric structures, leading to enhanced catalytic activities.[26–30] (iii) The uniformity of the electronic and geometric structure of the active sites in SACs endows them with similar spatial and electronic interactions with substrate molecules, which facilitates an improvement in the catalytic selectivity.[31,32] (iv) Furthermore, the structural simplicity and uniformity of the SACs are conducive to the characterization and identification of catalytic active sites, which enables SACs to serve as ideal models to study reaction mechanisms.[33–36] This also indicates opportunities to design and regulate the active sites of SACs at the atomic level.[37–42] (v) Specifically, in the electrochemical $CO_2RR$, atomically dispersed metal atoms are suitable for single or coupled proton-electron transfer, and enhance the $CO_2$ adsorption and activation, leading to a high selectivity for $C_1$ products.[43–46] Meanwhile, isolated metal atoms offer an individual single adsorption site for $CO_2$, thus $C_2^+$ products are more difficult to obtain on SACs.[47–49] Despite substantial efforts being made to fabricate various SACs, the principles of regulating the intrinsic electrocatalytic performance of the single-atom active sites still needs to be sufficiently investigated.[50–52]

*Yuanjun Chen received his BS degree from the College of Chemical Engineering at Beijing University of Chemical Technology in 2015, and his PhD degree from the Department of Chemistry, Tsinghua University in 2020 under the supervision of Prof. Yadong Li. His research interests focus on the syntheses and applications of functional nanocatalysts and single-atom site catalysts.*

*Dingsheng Wang received his BS degree from the Department of Chemistry and Physics, University of Science and Technology of China in 2004, and his PhD degree from the Department of Chemistry, Tsinghua University in 2009, under the supervision of Prof. Yadong Li. He did his postdoctoral research at the Department of Physics, Tsinghua University with Prof. Shoushan Fan. He joined the faculty of the Department of Chemistry, Tsinghua University in 2012.*

*Yadong Li received his B.S. degree from the Department of Chemistry at Anhui Normal University in 1986 and his Ph.D. from the Department of Chemistry at the University of Science and Technology of China in 1998. He joined the faculty of the Department of Chemistry at Tsinghua University in 1999. He was elected as a member of the Chinese Academy of Sciences in 2011.*

In this perspective article, we first focus on the controlled synthesis of SACs at the atomic scale for electrochemical $CO_2$ reduction reactions with regards to five aspects: regulation of the central metal atom, the coordination environment, the interface of single metal complex sites, multi-atom active sites and other ingenious strategies to improve the performance of the SACs. Finally, the challenges and potential for precise control over the synthesis and accurate characterization and identification of the active sites of SACs, as well as a study of the reaction mechanisms on electrochemical $CO_2$RR, will be discussed.

## 2. Design and synthesis of SACs for the $CO_2$RR

The active sites of SACs can be divided into central metal atoms and the surrounding coordination environment, the influences of which on the activity and selectivity will be discussed first. Then, we will focus on the kind of SACs that constitute anchored metal complexes with constructed structures on the substrates, which are different from the traditional SACs that involve the building of coordination structures on substrates by anchoring metal atoms. Moreover, as the active sites of traditional SACs are separated atomically, they are expected to be more favorable to the $C_1$ product. In the fourth section, we will discuss multi-atom active sites which have a huge potential to obtain $C_2^+$ products as they have multiple $CO_2$ adsorption sites which can introduce multiple $CO_2$ molecules into a single reaction. Finally, we will review other ingenious strategies to improve the $CO_2$RR performance of the SACs.

### 2.1 Regulation of the central metal

**2.1.1 Regulation of the central metal elements.** The central metal atoms are not only regarded as the essential constituents for traditional homogenous catalysts, but also play central roles in SACs. The electronic structures of active sites are largely based on different kinds of central metal and their different valence states. Gong *et al.* proposed an intrinsic descriptor ($\Phi$) correlated with the electronic state of the central metal, which can enable a metal–nitrogen–doped carbon (M–N–C) SACs catalytic performance in the $CO_2$RR.[53] $\Phi$ is defined as $\Phi = V_M \times E_M/r_M$, in which $V_M$, $E_M$, $r_M$ represents the valence electron number of metals, the electronegativity of the central metals, and the radius of the metal ions, respectively. By calculating $\Phi$, they predicted the $CO_2$RR performance sequence would be Co > Fe > Mn > Ni > Cu, which was successfully confirmed by the faradaic efficiency (FE) and the onset potential of the experimental results. This work highlighted that the choice of central metal is of great importance in the design of SACs for the $CO_2$RR from a computational perspective.

Although SACs based on noble metals have revealed a good activity and selectivity, the shortage of noble metal resources and their expensive price has motivated researchers to investigate non-noble metal SACs.[54,55] Cu and transition metals such as Fe, Ni, Co and so on are viewed as promising candidates because of their rich d orbital electrons and the variation in the valence state. Although the electrochemical $CO_2$RR has multiple products, CO, as the simplest one, is often used to evaluate the performance of the central metals. Li *et al.* investigated the different catalytic performances of metal–$N_x$ ($MN_x$, M = Mn, Fe, Co, Ni, and Cu) moieties on the M–N–C catalysts.[56] Catalytic experiments revealed a volcano trend between the atomic number of the tested metal and their electrochemical $CO_2$RR performance, which can be explained by the Gibbs free energy changes of the rate determined steps. Based on different electrochemical potentials, Fe and/or Co are located at the top of the volcano (Fig. 1a). In contrast, there is no obvious trend towards faradaic efficiency for CO. The high selectivity of Fe and Co ($FE_{CO}$ > 80%) can be explained by the binding energy of $CO_2^*$ and H*, which are associated with the electron number of d-antibonding. Ju *et al.* investigated the $CO_2$-to-CO electrochemical reduction catalytic performance of the M–N–C catalysts with different metal centers (M = Mn, Fe, Co, Ni, Cu).[40] Fe–N–C showed a maximum $FE_{CO}$ of 65% at −0.55 V *versus* RHE ($V_{RHE}$), and Ni–N–C exhibited a maximum $FE_{CO}$ of 85% at −0.78

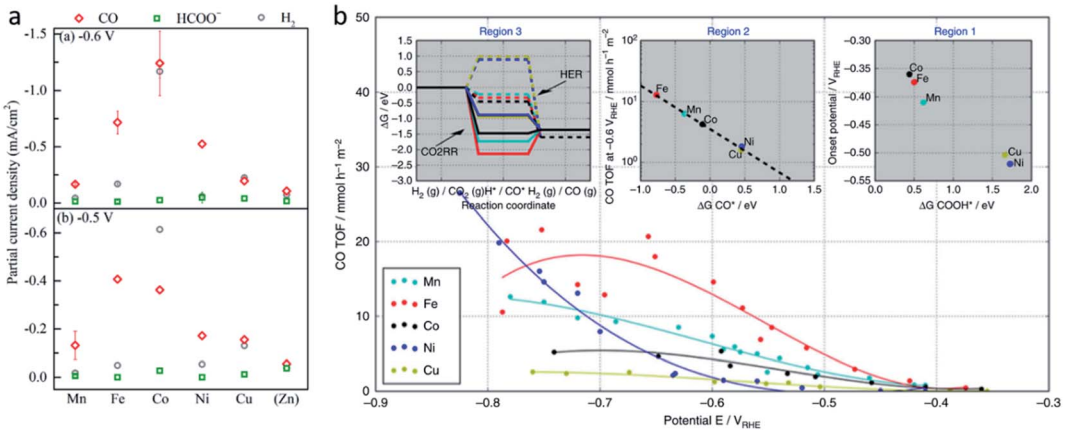


Fig. 1 (a) The volcano trend of M–N–C catalysts in terms of electrochemical $CO_2$RR performance. Partial current densities of M–N–C catalysts for CO, $HCOO^-$, and $H_2$ products at −0.6 $V_{RHE}$ and −0.5 $V_{RHE}$. Reproduced from ref. 56 with permission from the American Chemical Society, copyright 2019. (b) Experimental CO TOFs of M–N–C catalysts. Reproduced from ref. 40 with permission from Springer Nature, copyright 2017.

$V_{RHE}$. Combined with the density functional theory (DFT) calculations, Fe–N–C and Ni–N–C were predicted to be promising SACs for $CO_2$-to-CO (Fig. 1b). Zheng *et al.* developed a universal principle to synthesize a series of SACs–M–N–C (M = Fe, Co, Ni, Cu) using *in situ* pyrolysis.[57] The experimental results revealed Ni > Fe > Cu > Co as the catalytic performance sequence of SAs–M–N–C in electrochemical $CO_2$-to-CO conversion. They attributed this result to the intrinsic property of the pyrrole-type M–$N_4$ structures. Pan *et al.* synthesized the M–N–C (M = Fe, Co) catalysts with M–$N_4$ sites from the Fe- or Co-doped MOFs precursors.[58] Fe–N–C reached a maximum $FE_{CO}$ of 93% at −0.58 $V_{RHE}$, which is much higher than the maximum $FE_{CO}$ of Co–N–C, which was 45% at −0.59 $V_{RHE}$ (Fig. 2a and b). This experimental result is consistent with the results of the DFT calculations. In conclusion, regardless of the nuances which may be caused by different substrates, Ni and Fe showed the most promising catalytic activities among the M–N–C catalysts for the $CO_2$-to-CO electrochemical $CO_2$RR, which was verified using multiple experiments.[59–61]

Furthermore, different central metals have different binding energies with intermediates such as *CO, $*CO_2^-$, and *COOH, which may lead to different products. For example, a high *COOH binding energy and weak *CO binding energy leads to CO, the Sn, Pb species with low $*CO_2^-$ binding energy lead to formate or formic acid, and metallic Cu with an enhanced *CO and *COOH binding energy leads to hydrocarbons.[49,56,62] Zhang *et al.* synthesized N-doped porous carbon supported Cu single atom catalysts for electrochemical $CO_2$ reduction to acetone, which exhibited a maximum $FE_{acetone}$ of 36.7% at −0.36 $V_{RHE}$.[32] Han *et al.* designed microporous N-doped carbon supported Zn single atom catalysts for reducing $CO_2$ to $CH_4$, which reached a maximum $FE_{CH4}$ of 85% at −1.8 $V_{SCE}$.[45]

However, the design of SACs for complicated products is still hindered by complicated mechanisms and various by-products. With the help of theoretical calculations, some researchers have provided guidance for future experimental efforts. Cui *et al.* used DFT calculations and a computational hydrogen electrode (CHE) model to investigate $C_2N$–graphene supported SACs with 12 different metal centers (M@$C_2N$).[63] They conducted DFT calculations with the models of the metal atom confined in the $N_6$ cavity as the active sites. Among the 12 metals, Ti, Mn, Fe, Co, Ni, Cu, Rh, and Ru preferred the $CO_2$RR to the HER under 0 V (Fig. 2c). Furthermore, different M@$C_2N$ were predicted to produce methane (M = Ti, Mn) and methanol (M = Fe, Co, Ni, Ru), as their different carbophilicity and oxophilicity could determine the formation of the important intermediates $*CH_3O$ and $*CH_2OH$, leading to the products $CH_4$ and $*CH_3OH$, respectively.

In addition to the transition metals, some SACs with main group elements also reveal an excellent performance in the electrochemical $CO_2$RR. Zhang *et al.* prepared a Bi-single-atom catalyst supported on N-doped carbon networks (Bi SAs/NC) for $CO_2$ reduction to CO.[64] Bi SAs/NC was synthesized by a bismuth-based metal organic framework (MOF) and dicyandiamide (DCD) thermal decomposition. During the decomposition, Bi nanoparticles (NPs) were generated first, the ammonia

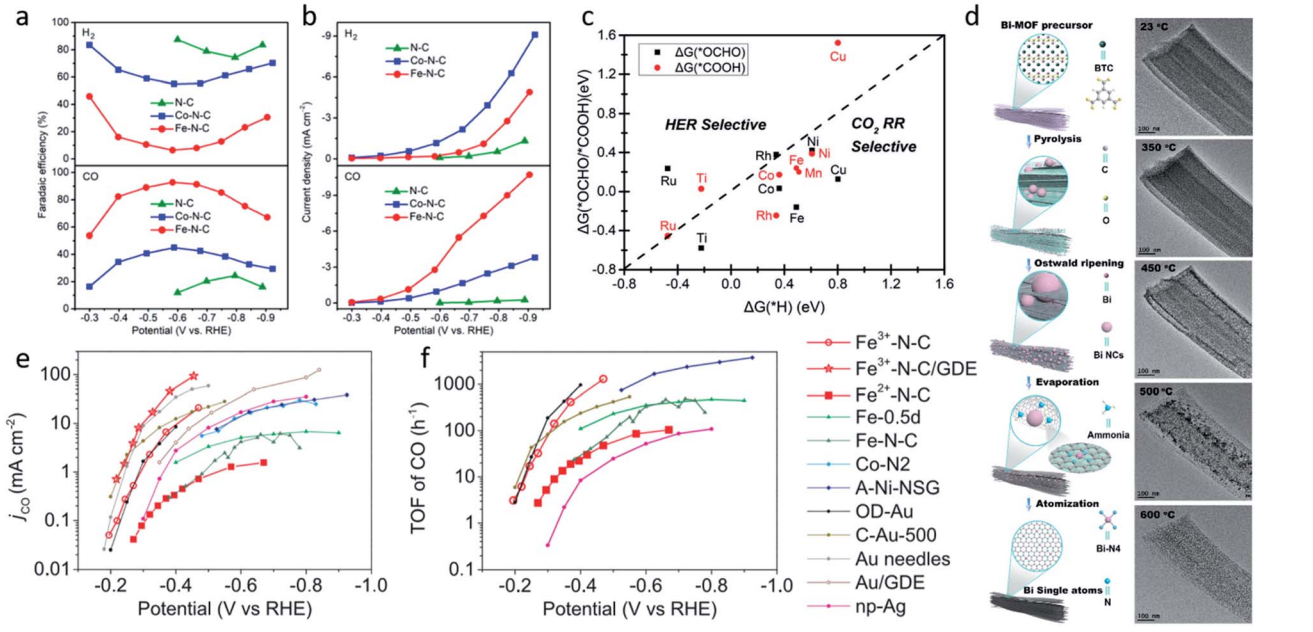


Fig. 2 The Faradaic efficiencies for CO and $H_2$ (a) and the current densities (b) of N–C, Co–N–C, and Fe–N–C. Reproduced from ref. 58 with permission from the American Chemical Society, copyright 2018. (c) Gibbs free energy changes for the first protonation step. Reproduced from ref. 63 with permission from The Royal Society of Chemistry, copyright 2018. (d) A schematic illustration of the process of Bi-MOF transformation to single Bi atoms and TEM images of Bi-MOF pyrolyzed at different temperatures. Reproduced from ref. 64 with permission from the American Chemical Society, copyright 2019. (e) CO current density ($j_{CO}$) and (f) apparent TOFs of CO production of $Fe^{3+}$–N–C and of $Fe^{2+}$–N–C in comparison with other reported catalysts. Reproduced from ref. 59 with permission from the American Association for the Advancement of Science, copyright 2019.

generated from DCD decomposition promoted the atomization of the Bi NPs (Fig. 2d). Under −0.5 $V_{RHE}$, Bi SAs/NC exhibits a maximum $FE_{CO}$ of 97%, and a current density of 3.9 mA $cm^{-2}$. DFT calculations illustrated that the Bi–$N_4$ sites act as the active centers, which promotes $CO_2$ activation and *COOH formation.

**2.1.2 Regulation of the central metal valence.** Another determining factor for the electronic structure of SACs is the valence of the central metal. Gu *et al.* prepared $Fe^{3+}$–N–C by pyrolysis of Fe-doped ZIF-8 in $N_2$ at 900 °C.[59] The Fe ions maintain a +3 oxidation state during electrocatalysis, which was confirmed by operando X-ray absorption spectroscopy. Spectroscopic characterization confirmed the $Fe^{3+}$ ions coupled electronically with pyrrolic N, resulting in a $Fe^{3+/2+}$ lower reduction potential, leading to the stabilization of $Fe^{3+}$. Catalytic experiments revealed $Fe^{3+}$–N–C had a lower onset overpotential, higher turnover frequency (TOF) and better stability than $Fe^{2+}$–N–C, which could be explained by the weaker CO binding with $Fe^{3+}$ (Fig. 2e and f). Yang *et al.* prepared low-valence Ni(+1) SACs that exhibited a high catalytic performance in $CO_2$-to-CO electrochemical reduction.[26] The experimental and DFT calculation results illustrated the delocalization of the unpaired electron in the Ni $3d_{x^2-y^2}$ orbital and the overlap between the Ni $3d_{x^2-y^2}$ and C 2p orbital promoted the formation of $CO_2^{\delta-}$ species. Numerous studies have revealed that SACs with a unique valence metal center can deliver an excellent catalytic performance in $CO_2$ reduction, the characterization of the valence of the central metal ions is still limited. As the valence may change during the catalysis, significant efforts should be made to develop operando characterization. Also, the electronic metal-support interaction (EMSI) between the central metal atoms and coordinated atoms plays an important role in determining the valence of the single metal atoms, which will be introduced in the next section.[65]

## 2.2 Regulation of the coordination environment

**2.2.1 Short-range regulation.** The surrounding coordination environment is another important factor in manipulating the intrinsic nature of single atom sites in SACs. As aforementioned, it has a strong relationship with the valance state of the central atoms. The unique coordination structure of SACs supported on a well-designed substrate surface gives opportunities to construct central metal atoms with unique valances. Many studies have focused on Ni-single-atom catalysts with a +1 oxidation state.[26,34,66–68] The average +1 oxidation state of Ni in the NC-carbon nanotubes (CNTs) (Ni) was between the metallic state Ni(0) and oxidized state Ni(+2), which can be explained by the electronic interaction between the central metal atoms and the neighboring atoms.[68]

The coordination atoms, coordination number and coordination steric structure are the main influencing factors in the coordination environment of the single-atom sites, and these play important roles in regulating the electronic and geometric structures of the single-atom sites. Different coordination atoms directly influence the strength of the EMSI, changing the valence electron distribution of single-atom sites, thus leading to a different catalytic performance for the $CO_2$RR. Nitrogen atoms are the most common coordination atoms owing to the significant development of M–N–C catalysts.[69–74] Therefore,

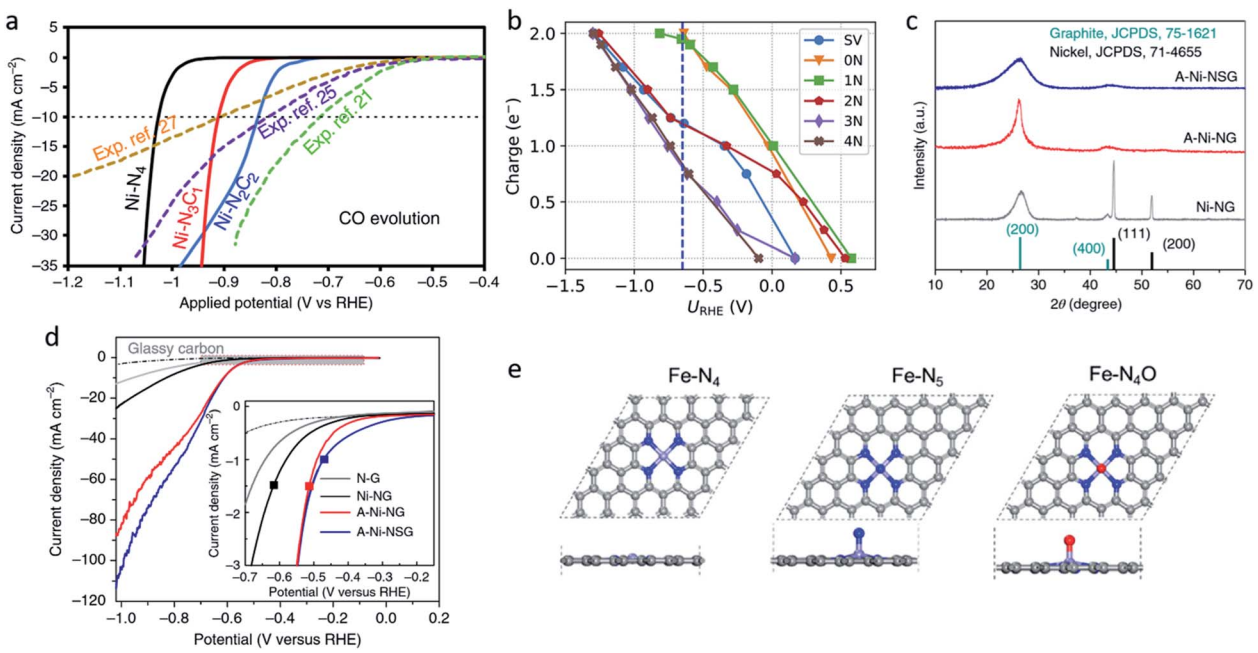


Fig. 3 (a) Calculated $j_{CO}$ values in the $CO_2$RR on Ni–$N_2C_2$, Ni–$N_3C_1$, and Ni–$N_4$. Reproduced from ref. 75 with permission from Springer Nature, copyright 2020. (b) Charge capacities of different sites under different potentials for *COOH. Reproduced from ref. 77 with permission from the American Chemical Society, copyright 2020. (c) XRD patterns and (d) LSV curves for A-Ni-NSG, A-Ni-NG, and Ni-NG. Reproduced from ref. 26 with permission from Springer Nature, copyright 2018. (e) Top views and side views of the Fe–$N_4$, Fe–$N_5$ and Fe–$N_4O$ sites. Reproduced from ref. 78 with permission from Elsevier, copyright 2020.

plenty of studies have investigated the hybrid coordination environment of the nitrogen and carbon atoms. Hossain *et al.* explored a series of Ni-single-atom catalysts with different N and C hybrid coordination environments of the Ni sites (Ni–$N_2C_2$, Ni–$N_3C_1$, Ni–$N_4$) on a graphene support.[75] The grand canonical potential kinetics (GCP-K) methodology was developed to predict their catalytic activities for $CO_2$ reduction to CO and $H_2$ production. The prediction revealed the HER performance is correlated with the number of coordinated C atoms, indicating Ni–$N_4$ is least favorable for HER. Ni–$N_4$ exhibited the best performance for $CO_2$ reduction, reaching 40 mA $cm^{-2}$ with $FE_{CO} \approx 100\%$ at $-1.05$ $V_{RHE}$ (Fig. 3a). Research on $Co_1$–$N_{4-x}C_x$ conducted by Geng *et al.* reported similar results.[76] Their study revealed that compared to $Co_1$–$N_{4-x}C_x$, $Co_1$–$N_4$ exhibited a higher binding strength with $CO_2$. This resulted in the easier activation of $CO_2$, and led to a higher current density and TOF of $Co_1$–$N_4$. However, other studies may come to a different conclusion. Zhao *et al.* applied *ab initio* molecular dynamics (AIMD) to investigate the catalytic kinetics of Ni-single-atom catalysts supported by N-doped graphene toward $CO_2$-to-CO electrochemical reduction *via* a "slow-growth" sampling approach.[77] Calculations predicted that the higher Fermi level of the Ni–$N_4$ site at the charge-neutral state led to its lower capacity, suggesting its higher electrochemical barriers and lower activity. The activity of Ni–$C_4$ and Ni–$C_3N_1$ sites differs by the CO desorption energy, the lower desorption barrier of the Ni–$C_3N_1$ sites, resulting in its higher activity. As a result, the coordination environment with one nitrogen and three carbon atoms is believed to have the best activity and selectivity for $CO_2$RR (Fig. 3b). The different results could be attributed to several factors. Firstly, the different calculation models, which focused on different rate determined steps and are inaccurate compared to the real experiment. Secondly, the different catalytic activity evaluation indicators, such as the FE, current density, TOF, and so on. Moreover, the different substrates and their synthesis process may also influence the activity, even though single-atom sites have a similar composition.

Oxygen and sulphur atoms, which are electron-rich and easy to dope, can also be introduced to the hybrid coordination environment. The hybrid coordination environment not only regulates the electronic structure of single-atom sites, but also creates defects on the substrate, leading to a better catalytic activity and stability. Yang *et al.* reported a Ni single-atom site catalyst supported on N,S-doped graphene (A-Ni-NSG) and N-doped graphene (A-Ni-NG).[26] The weaker and wider X-ray diffractometry (XRD) peaks indicated A-Ni-NSG has a defect-rich structure compared to A-Ni-NG (Fig. 3c). Multiple characterizations revealed the existence of Ni–S bonds in A-Ni-NSG. Compared to A-Ni-NG, A-Ni-NSG exhibited a lower onset overpotential, larger current density and better chemical stability, suggesting the introduction of S atoms into the coordination environment improved the catalytic activity (Fig. 3d). Wang *et al.* synthesized a nanoporous carbon supported Fe single-atom catalyst with a Fe–$N_4O$ structure.[78] The extended X-ray absorption fine structure (EXAFS) wavelet transform (WT) results confirmed the existence of Fe–O. In the Fe–$N_4O$ structure, four N atoms were coordinated in a planar position to Fe, while the O atom was coordinated out-of-plane (Fig. 3e). This coordination structure was optimized using DFT calculations as the lowest free energy structure. DFT calculations also revealed the CO desorption barrier on Fe–$N_4O$ is relatively low, leading to easier CO desorption and alteration of the rate determining step (RDS). The RDS changed from *CO-to-CO to $CO_2$-to-*COOH, indicating that Fe–$N_4O$ had a better performance at a high overpotential. The Fe–$N_4O$ catalyst reached $FE_{CO} \approx 96\%$ at $-0.57$ $V_{RHE}$, suggesting the Fe–$N_4O$ structure could be a promising direction for designing M–N–C $CO_2$RR catalysts. Also, there are some novel coordination structures, such as the $\pi \rightarrow$ d coordination interactions which are not viewed as an atom coordination, but as a bond coordination instead. Shen *et al.* reported the novel structure of a triphenylene–graphdiyne supported Cu-single-atom catalyst (Cu@TP-GDY) using DFT calculations.[79] The DFT calculations unveiled the atomically dispersed Cu species were confined in triangular pores by $\pi \rightarrow$ d interactions between diacetylenic linkages and Cu atoms. $CO_2$-to-COOH* was predicted to be the rate determined steps on Cu@TP-GDY. Cu@TP-GDY was expected to show a better catalytic performance towards $CO_2$RR, as its overpotential was found to be lower than most of the Cu-based catalysts.

The change of the coordination number also significantly affects the activity of single-atom sites, which will not only influence the geometric structure, but also reattribute the electronic structures, leading to different catalytic performances. Fan *et al.* constructed a Ni single atom catalyst (NC-

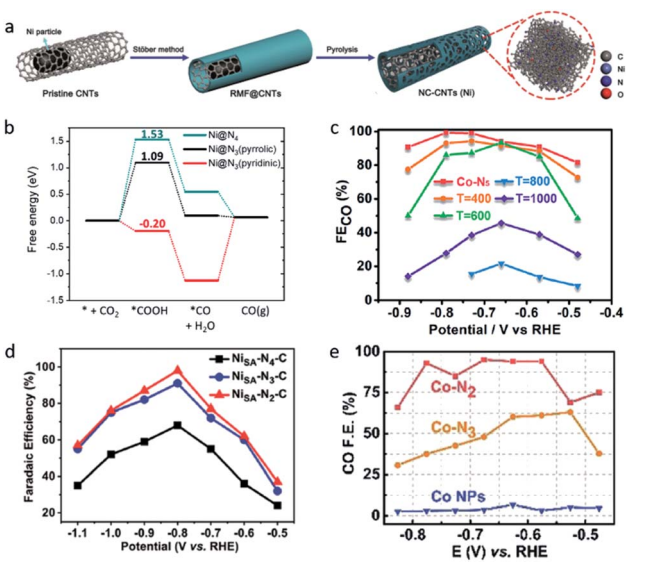


Fig. 4 (a) A schematic illustration of the formation of NC-CNTs (Ni). (b) Free energies of the $CO_2$RR to CO on Ni@$N_4$ and Ni@$N_3$. Reproduced from ref. 68 with permission from John Wiley and Sons, copyright 2019. (c) $FE_{CO}$ values of Co–$N_5$/HNPCSs-T at different applied potentials. Reproduced from ref. 35 with permission from the American Chemical Society, copyright 2018. (d) $FE_{CO}$ values of Ni–$N_x$–C SACs ($x$ = 2,3,4) at different applied potentials. Reproduced from ref. 38 with permission from John Wiley and Sons, copyright 2019. (e) $FE_{CO}$ values of Co–$N_x$ SACs ($x$ = 2,3,4) at different applied potentials. Reproduced from ref. 39 with permission from John Wiley and Sons, copyright 2018.

CNTs (Ni)) through the pyrolysis of Ni particles containing commercial multi-walled carbon nanotubes (MWCNTs) coated with a polymeric layer (Fig. 4a).[68] EXAFS fitting results indicated the Ni–N coordination number is 2.5 ± 0.2. The authors viewed $NiN_3$ moieties as the active center in the NC-CNTs (Ni). DFT calculations revealed the formation of *COOH has a lower free energy on $NiN_3$ (pyrrolic) than on $NiN_4$, which means the NC-CNTs (Ni) exhibit a better catalytic performance for electrochemical $CO_2$-to-CO conversion (Fig. 4b).

The most common strategy to create SACs with a lower coordination number is high temperature pyrolysis. Pan *et al.* synthesized polymer-derived hollow N-doped porous carbon spheres (HNPCSs) supported Co–$N_5$ sites catalysts.[35] Cobalt phthalocyanines are uniformly anchored on the HNPCSs, together with the strong electronic interactions which were revealed by Raman spectroscopy. As the pyrolysis temperature was raised to 400 and 600 °C, the $FE_{CO}$ of Co–$N_5$/HNPCSs dropped and the coordination number decreased to 4 and 3 (Fig. 4c). The Co–$N_5$/HNPCSs catalyst exhibited a high $FE_{CO}$ (>90%) over a wide potential range (−0.57–0.88 $V_{RHE}$), which can be attributed to the low *COOH formation free energy and moderate binding energy of CO on the Co–$N_5$ sites. In contrast, a negative correlation between the N coordination numbers and catalytic activity was reported. In research published by Gong *et al.*, a series of N-doped carbon supported Ni SACs (Ni–$N_x$–C, $x$ = 2,3,4), Ni–$N_2$–C achieved the highest $FE_{CO}$ of 98% and the highest TOF of 1622 $h^{-1}$ (Fig. 4d).[38] Wang *et al.* reported Co single-atom catalysts on N-doped porous carbon (Co–$N_x$ SACs, $x$ = 2, 3, 4), the Co–$N_2$ SACs exhibited a high $FE_{CO}$ of 94% and a high current density (Fig. 4e).[39] The uncertain correlation between the N coordination numbers and the catalytic performance in a different series of SACs may be explained by their different coordination structures, owing to the different synthesis processes. Co–$N_x$/HNPCSs ($x$ = 3, 4) was obtained by the pyrolysis of Co–$N_5$/HNPCSs, while Ni–$N_x$–C SACs ($x$ = 2, 3, 4) and Co–$N_x$ SACs ($x$ = 2, 3, 4) were obtained by the pyrolysis of the MOFs precursors under different temperatures.

Although it is difficult to control the coordination number exactly using the pyrolysis method, some well-designed strategies have been developed to produce SACs with a defined coordination number. Rong *et al.* developed a strategy to synthesize vacancy-defect Ni SACs (Ni–$N_3$–V).[37] They first prepared Ni–$N_3$O single-atom catalysts under 500 °C. As the temperature rises, the coordinated oxygen atom on the substrate can be gradually evaporated leaving vacancy-defects, thus the Ni–$N_3$–V SACs were formed (Fig. 5a). The structure of the Ni–$N_3$–V sites was confirmed using Fourier transform (FT)-EXAFS fitting in the R space. At −0.9 $V_{RHE}$, Ni–$N_3$–V exhibited a high $FE_{CO}$ of 90%, a high current density of 65 mA $cm^{-2}$ and a high TOF of 1.35 × $10^5$ $h^{-1}$. DFT calculations were performed on Ni–$N_4$, Ni–$N_3$, (in which the Ni atom was coordinated with three nitrogen atoms and exhibited a symmetrical structure) and Ni–$N_3$–V (in which the Ni atom was coordinated with three nitrogen atoms and a vacancy, and exhibited an asymmetrical structure). Ni–$N_3$–V and Ni–$N_3$ both exhibited a lower free energy in the RDS (the formation of *COOH), but Ni–$N_3$ encountered difficulties when releasing the CO, suggesting the vacancy-defect structure in Ni–$N_3$–V greatly promoted the catalysis of $CO_2$ reduction. Zhang *et al.* reported structured $FeN_5$ SACs on the N-doped graphene support through the pyrolysis of hemin and melamine.[28] A large amount of melamine was added, which served as a nitrogen source to promote the formation of Fe–$N_5$ sites. The N atoms in the adjacent layers provided axial ligand sites for $FeN_4$ to convert to $FeN_5$ (Fig. 5b). The $FeN_5$ catalyst showed a greater performance towards $FeN_4$ in $CO_2$-to-CO conversion owing to the *CO weaker binding strength on $FeN_5$, and reached a maximum $FE_{CO}$ of 97.0% at −0.46 $V_{RHE}$.

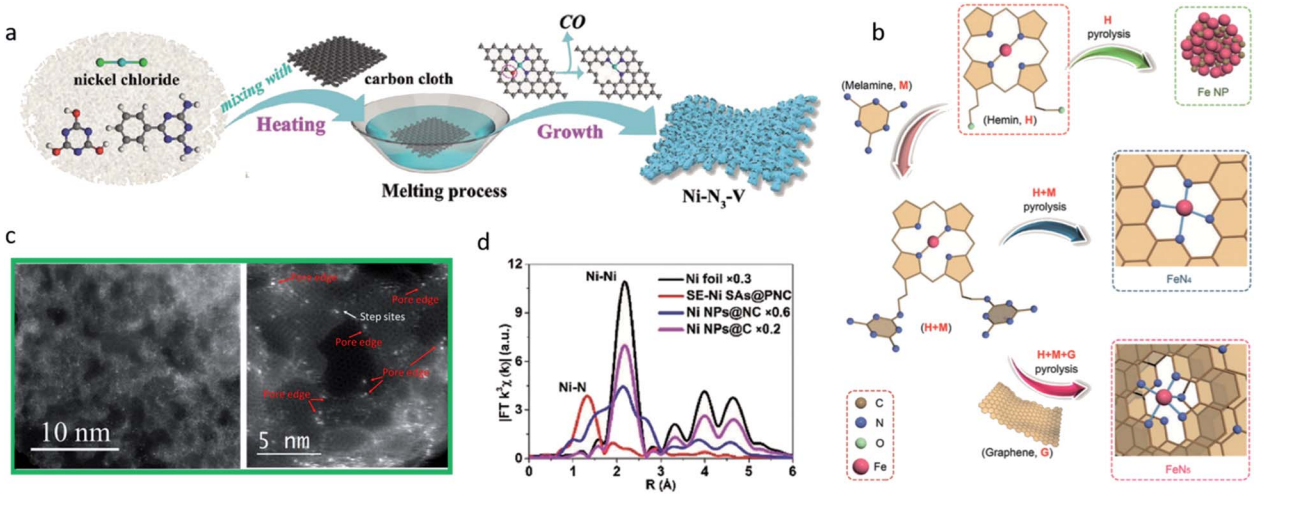


Fig. 5 (a) A schematic illustration of the synthesis of Ni–$N_3$–V. Reproduced from ref. 37 with permission from John Wiley and Sons, copyright 2020. (b) A schematic illustration of the synthesis of $FeN_4$ and $FeN_5$ SACs. Reproduced from ref. 28 with permission from John Wiley and Sons, copyright 2019. (c) AC-STEM images of Ni–N-MEGO illustrating that the single atoms of Ni are predominately anchored on the edges of the nanopores. Reproduced from ref. 80 with permission from Elsevier, copyright 2018. (d) FT-EXAFS spectra of Ni foil, SE-Ni SAs@PNC, Ni NPs@NC, and Ni NPs@C. Reproduced from ref. 81 with permission from John Wiley and Sons, copyright 2018.

The effect of the coordination steric structure towards active sites is often overlooked because of its close connection with the coordination atoms and coordination number.[78] However, it is of great importance to investigate the appropriative coordination steric structure. This provides a new strategy to regulate the electronic structure, directly modifying the accessibility of the single-atom sites, and eventually improving the selectivity and activity. Cheng *et al.* developed microwave exfoliated graphene oxide supported Ni SACs (Ni–N-MEGO).[80] Aberration-corrected scanning transmission electron microscopy (AC-STEM) combined with X-ray absorption spectroscopy (XAS) indicated the atomically dispersed Ni atoms were anchored on the edges of nanopores (Fig. 5c). The DFT calculations suggested the three N coordinated edge-anchored Ni sites have a better performance than in-plane structures owing to their moderate $CO_2$ activation energy and CO desorption energy.

In addition to all the aforementioned improvements in the catalytic performance, the rational design of the coordination environment can also contribute to the synthesis process, and even improve the durability of SACs. Yang *et al.* investigated the process of defect-containing N-doped carbon supported Ni NPs converted to Ni single atoms through thermal atomization.[81] Aberration corrected high-angle annular dark-field scanning transmission electron microscope (HAADF-STEM) measurements and environmental transmission electron microscopy (TEM) were employed to characterize the process. The average size of the Ni NPs was gradually increased as the temperature rose. When the temperature was above 673 K, the Ni NPs started the atomization process, distributed to Ni single atoms. EXAFS revealed the dominant peak of Ni–N at 1.32 Å appeared after the thermal process, while the Ni–Ni peak at 2.15 Å disappeared, suggesting the Ni–N strong coordination promoted the Ni NPs atomization process (Fig. 5d).

**2.2.2 Long-range regulation.** Despite the first shell coordination atoms having the strongest EMSI, the higher shell atoms also sometimes play an important part in the promotion of the catalytic performance. Some regulations of atoms around the coordination environment can be viewed as a co-catalysis or relatively independent active site to accelerate the rate determined steps or promote the side reactions, though these do not regulate the electronic structure of the central metals directly. Pan *et al.* explored two different kinds of $Ni–N_4$ moieties: the $Ni–N_{2+2}–C_8$ type at the edge of the carbon matrix and the $Ni–N_4–C_{10}$ type in the bulk of the carbon matrix (Fig. 6a).[82] The DFT calculations indicated the $Ni–N_{2+2}–C_8$ site with dangling bonds for active C atoms was viewed as the active moiety because of its lower activation energy for *COOH → *CO + *OH. In contrast, the bulk-hosted $Ni–N_4–C_{10}$ site seemed to be inactive, which could be explained by the fact that it was embedded in a graphitic layer. Previous work published by Pan *et al.* pointed out that the critical difference between two types of $M–N_4$ is that the adjacent carbon atoms of the $M–N_{2+2}–C_8$ types have dangling bonds, while the adjacent carbon atoms of $M–N_4–C_{10}$ have not.[58] DFT calculations revealed that after one of the C=O bonds breaks, the product, CO, is adsorbed on the M site, while OH is adsorbed on the dangling bonds of the adjacent C atom.

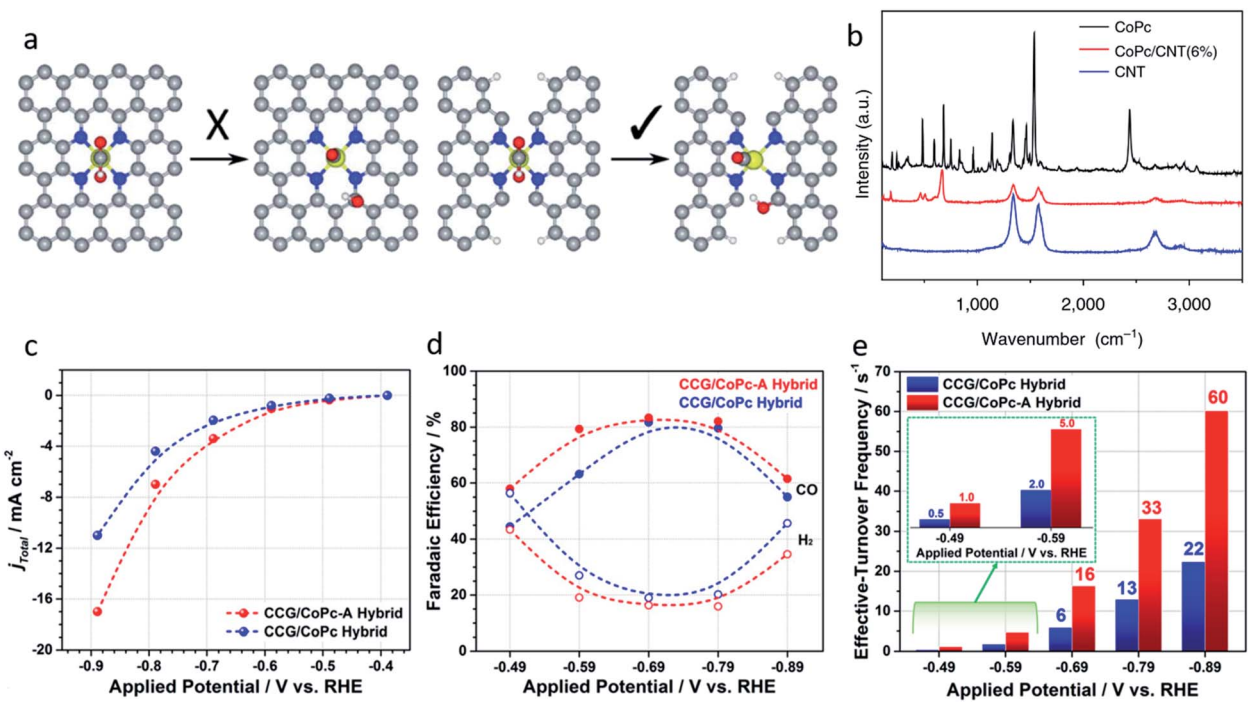


Fig. 6 (a) $Ni–N_4–C_{10}$ sites (left) are inactive for the *COOH dissociation reaction, $Ni–N_{2+2}–C_8$ sites are active because of the dangling bonds on the adjacent C atoms. Reproduced from ref. 82 with permission from the Royal Society of Chemistry, copyright 2019. (b) Raman spectra of CoPc, the CoPc/CNT(6%) hybrid, and CNTs. Reproduced from ref. 31 with permission from Springer Nature, copyright 2017. (c) Total current density, (d) faradic efficiencies, and (e) effective turnover frequencies of CCG/CoPc-A and CCG/CoPc hybrids. Reproduced from ref. 85 with permission from the American Chemical Society, copyright 2019.

This result supports the lower energy of the *COOH dissociation on the M–$N_{2+2}$–$C_8$ sites, leading to its high catalytic performance. In addition to the C atoms, uncoordinated N atoms, as a rich species on the M–N–C catalysts, may also serve as independent active centers. In the research reported by Song *et al.*, SACs with Co–$C_2N_2$ moieties were synthesized by the pyrolysis of ZnO@ZIF to catalyze both the $CO_2$RR and HER.[33] At −0.7 $V_{RHE}$ to 1.0 $V_{RHE}$, it exhibited an almost 100% $FE_{CO}$ and an ideal CO/$H_2$ ratio of 1/2. Potassium thiocyanate (KSCN) poisoning experiments and DFT calculations confirmed that the Co–$C_2N_2$ moieties served as the active sites for $CO_2$RR, while the additional N functional groups served as the active sites for HER.

### 2.3 Interface design of the single metal complexes

Traditional SACs were synthesized through anchoring metal atoms on the prepared substrate with coordination atoms to construct a coordination structure such as M–$N_4$, which was proved to be analogous to molecular catalysts.[83] Recently, a novel strategy was reported to synthesize SACs by anchoring metal complexes with a formed M–$N_4$ structure on a carbon substrate.[84] The M–$N_4$ structure in the metal precursor can integrally anchor on the substrate, leading to the formation of SACs with well-defined active sites. Also, as the metal complexes offer M–$N_4$, there is no need for the substrate to provide extra coordination atoms, therefore carbon materials (*e.g.*, graphene, carbon nanotubes, and MOFs) have become the most popular substrates in metal complex derived SACs. Metal phthalocyanine is a promising candidate for this kind of synthesis strategy. Zhang *et al.* anchored a cobalt phthalocyanine (CoPc) molecule on a carbon nanotubes (CNT) to synthesize a CoPc/CNT catalyst.[31] Inductively coupled plasma mass spectrometry (ICP-MS) demonstrated the amount of Co in the prepared CoPc/CNT was 0.63 wt%. Material characterizations also revealed the C and N of CoPc was distributed on the sidewalls of the CNTs that overlapped with the nanotube structures. Some of the vibrational modes of the CoPc are prohibited, indicting the strong electronic interaction between CoPc and CNT (Fig. 6b). CoPc/CNT exhibited a high activity, stability and selectivity in the $CO_2$-to-CO conversion. The phthalocyanine molecule offers several sites for organic modification, leading to improvements in the catalytic performance. The researchers further prepared a CoPc-CN/CNT hybrid catalyst using cobalt-2,3,7,8,12,13,17,18-octacyano-phthalocyanine (CoPc-CN). CoPc-CN/CNT delivered an even better catalytic performance for the $CO_2$-to-CO electrochemical reaction than CoPc/CNT. CoPc-CN/CNT maintained a $FE_{CO}$ value of over 95% at −0.53–0.63 $V_{RHE}$. Choi *et al.* anchored cobalt(+2) *octa*-alkoxy phthalocyanine (CoPc-A) on chemically converted graphene (CCG) *via* π–π stacking.[85] Compared to the graphene supported cobalt phthalocyanine catalyst (CCG/CoPc), the *octa*-alkoxy groups on phthalocyanine helped to suppress its aggregation, leading to its significantly enhanced catalytic activity. CCG/CoPc-A exhibited a higher total current density, a higher $FE_{CO}$, higher eTOFs for CO production and over 30 h of stable CO conversion (Fig. 6c–e). As with the other SACs, the metal loading will largely effect the performance

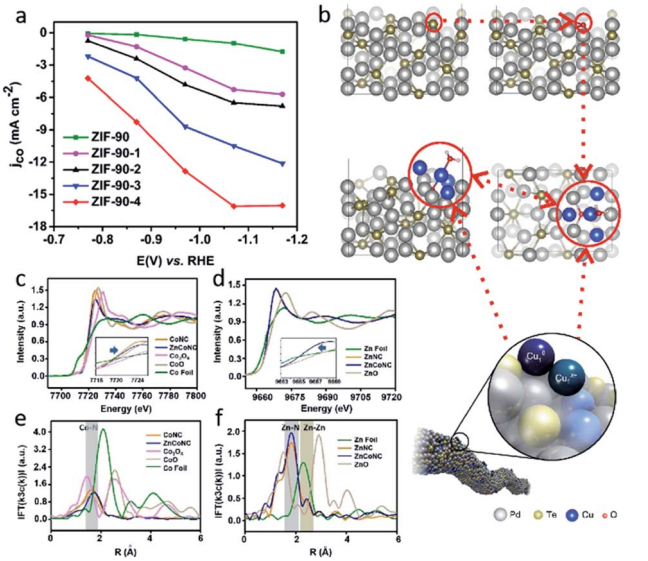


Fig. 7 (a) $j_{CO}$ values of ZIF-90, ZIF-90-1, ZIF-90-2, ZIF-90-3, and ZIF-90-4. Reproduced from ref. 86 with permission from the Royal Society of Chemistry, copyright 2020. (b) A schematic illustration of Cu-doped $Pd_{10}Te_3$ nanowires. Reproduced from ref. 91 with permission from Springer Nature, copyright 2019. Co (c) K-edge XANES and (e) Fourier-transform EXAFS spectra of ZnCoNC. Zn (d) K-edge XANES and (f) Fourier-transform EXAFS spectra of ZnCoNC. Reproduced from ref. 27 with permission from John Wiley and Sons, copyright 2020.

of the catalysts. Yang *et al.* synthesized a CoTAPc–ZIF-90 hybrid catalyst through anchoring cobalt phthalocyanine on the surface of ZIF-90 using the Schiff base reaction.[86] The SEM images confirmed the CoTAPc units were distributed uniformly, and the XANES spectra demonstrated the Co–$N_4$ structure. Catalytic control experiments revealed the catalytic performance of CoTAPc–ZIF-90, which was quantified by the CO partial current density, could be improved by increasing the content of CoTAPc from ZIF-90 (0 mg CoTAPc) to ZIF-90-4 (30 mg CoTAPc) (Fig. 7a). ZIF-90-4, synthesized using 30 mg of CoTAPc and 100 mg of ZIF-90, exhibited a high $FE_{CO}$ of 90% at −0.97 $V_{RHE}$ and a large current density of 13 mA $cm^{-2}$.

Additionally, the catalytic performance of the phthalocyanines derived SACs with different metal centers was investigated. Wang *et al.* reported a series of SACs (Me-SAC (Pc), Me = Co, Fe, Ni) for $CO_2$RR, synthesized by the pyrolysis of the encapsulating cyano-substituted metal phthalocyanines (MePc-CN) in Zeolitic imidazolate frameworks (ZIFs).[87] Me–N/C could enable metal loading up to approximately 2.2 wt% without aggregation. The sequence of the Me-SAC (Pc) current densities under certain potentials in the H-cell is Co-SAC (Pc) > Fe-SAC (Pc) > Ni-SAC (Pc). In the gas-diffusion electrode (GDE) setups, Ni-SAC (Pc) operated steadily from −10 up to −200 mA $cm^{-2}$ with a $FE_{CO}$ of over 96.0%, while Fe-SAC (Pc) only exhibited 50.1% of $FE_{CO}$ at −100 mA $cm^{-2}$. The results suggested the promising potential of Ni-SAC (Pc) for use in practical electrochemical $CO_2$RR devices.

In addition to metal phthalocyanines, some other molecular complexes, such as metal porphyrins, also have a defined M–$N_4$

structure. Kim *et al.* reported carbon substrate supported Ni molecular complexes with two different porphyrins ligands, tetraphenylporphyrin ($N_4$–TPP) and 21-oxatetraphenylporphyrin ($N_3O$-TPP)[88] Spectroscopic and computational studies of Ni–$N_4$-TPP and Ni(–Cl)–$N_3O$-TPP revealed that the destruction of the ligand field symmetry could increase the redox potential from 0 to +1, leading to a better performance in the $CO_2$RR. The additional ligand for the central atoms could also be a modification strategy to regulate the interfacial electronic structure from the axial direction. Wang *et al.* immobilized tetraphenylporphyrin cobalt (PCo) on graphene by π–π interactions only[89] They discovered that diphenyl sulfide (Di-S) could act as an axial ligand to the Co single atom sites. Di-S enhanced the electron transfer between the interface of graphene and Co complexes by parallel stacking geometry, leading to better generation of $[PCo]^{\cdot -}$ as active sites for $CO_2$RR.

Compared with the traditional synthesis of SACs, using metal complexes such as metal phthalocyanines and metal porphyrins as precursors shows several advantages. First, metal complexes can be anchored by π–π stacking without pyrolysis. Second, the M–$N_4$ structure in the metal complexes can be anchored onto the substrate intact to form SACs with clear active sites. Third, the steric hindrance of the phthalocyanine and porphyrin ring are large enough to alleviate the aggregation of the single atoms. Overall, the interface design of the single metal complexes offers a novel method for the construction of SACs and a bridge to connect molecular homogenous catalysts with heterogonous catalysts directly.

### 2.4 Design of multi-atom site catalysts

Although SACs exhibit a great performance in the $CO_2$RR, most of them catalyze reactions that only involve single molecules. On traditional SACs, the single metal atoms are dispersed on substrates in isolation with no interaction between each other. When the neighboring single atom is close enough, there is a chances that C–C coupling reactions will be enabled, leading to $C_2^+$ products. Guan *et al.* reported electrochemical $CO_2$ reduction to $C_2H_4$ on single-atom Cu catalysts supported on nitrogen-doped carbon.[90] When the Cu concentration was below approximately 2.4%$_{mol}$, the Cu–$N_x$ species were isolated, leading to the $C_1$ products of $CH_4$. When the Cu concentration reached approximately 4.9%$_{mol}$, the adjacent Cu–$N_x$ species was close enough to enable a synergistic effect between the neighboring Cu single atoms and resulted in the dimerization of the *CO intermediates. If the distance between the single-atom site continues to reduce, the extreme condition of it will result in multi-atoms site catalysts. Several multi-atoms site catalysts have been reported in recent research, in which the active sites were constructed by two or more metal atoms instead of only one metal atom in the SACs. The multiple atoms offer additional sites for $CO_2$ adsorption, involving additional $CO_2$ in a single reaction process, and leading to the production of $C_2^+$ products. Jiao *et al.* reported a Cu atom-pair catalyst (Cu-APC) on $Pd_{10}Te_3$ nanowires for the $CO_2$ electrochemical reduction to CO.[91] By combining the EXAFS and DFT calculations, they revealed that in $Cu_4$, which is the smallest stable configuration, $Cu_1^{x+}$ was formed *via* a single Cu atom binding with an O atom, then a $Cu_1^0$–$Cu_1^{x+}$ atom pair was constructed as an active site by $Cu_1^{x+}$ together with an adjacent Cu atom (Fig. 7b). Further calculations indicted that the $Cu_1^0$–$Cu_1^{x+}$ sites catalytic mechanism is a 'biatomic activating bimolecular' mechanism. At −0.78 $V_{RHE}$, Cu-APC with a 0.10% Cu loading exhibited a $FE_{CO}$ of 92%, with only a corresponding $FE_{H_2}$ of 3%. The theoretical calculation also confirmed that diatomic sites catalysts promote the formation of $C_2^+$ products. Zhao *et al.* investigated whether the porous $C_2N$ layer supported a series of transition metal dimers catalysts ($Cu_2$@$C_2N$) for $CO_2$RR using DFT calculations.[92] The results showed a maximum positive free energy change of 0.76 eV in the formation of the COCO* species, indicating that $Cu_2$@$C_2N$ is preferred to $C_2H_4$ in the $CO_2$RR.

In addition, multi-atoms sites can be constructed using different transmission metal atoms. Zhu *et al.* reported neighboring Zn/Co monomers dispersed on N doped carbon (ZnCoNC) for electrochemical $CO_2$ reduction to CO.[27] The indirect electron interaction of the neighboring Zn/Co through the N atoms was confirmed using XANES and EXAFS analysis (Fig. 7c–f). *In situ* attenuated total reflection-infrared spectroscopy (ATR-IR) and DFT calculations suggested that the electronic effect of the neighboring Zn/Co reduced the *COOH formation energy barrier, leading to easier CO production. ZnCoNC exhibited a $FE_{CO}$ of 93.2% at −0.5 $V_{RHE}$ in a 30 h test. Ren *et al.* synthesized a diatomic Ni–Fe sites catalyst supported by nitrogenated carbon (Ni/Fe–N–C) *via* an ion-exchange strategy.[93] The obvious metal–metal peak for Ni–Fe coordination was observed at 2.06 Å in FT EXAFS spectra. Compared with Ni–N–C and Fe–N–C synthesized using similar methods, Ni/Fe–N–C exhibited a higher faradaic efficiency of CO, a higher current density of CO, and a higher TOF. Moreover, the Ni/Fe–N–C reached a maximum $FE_{CO}$ of 98% at −0.7 $V_{RHE}$, and maintained a $FE_{CO}$ of 99% after 30 h of continuous electrolysis, suggesting its outstanding catalytic performance and durability. DFT calculations revealed the diatomic Ni–Fe sites of Ni/Fe–N–C provided an additional active site for the second $CO_2$ activation. Compared with bare Ni/Fe–N–C, CO-adsorbed Ni/Fe–N–C has a weaker binding strength for COOH* and CO*, leading to a lower energy barrier for CO production.

Apart from dual-atom site catalysts with metal–metal bonds, there are some dual-atom site catalysts which are composed of two types of single-atomic sites with two different metal centers. Xie *et al.* reported hierarchical integrated electrodes supported NiSn atomic pair catalysts (NiSnAPC).[94] XAFS and XPS analysis suggested that NiSnAPC contains a separately dispersed Ni–$N_4$ and Sn–$N_4$ configuration and the Ni–Sn bond was not observed. However, the isolated Ni–$N_4$ and Sn–$N_4$ configuration could allow them to modify each other's electronic structure. Compared with Sn-SAC, NiSn-APC exhibited a TOF of 4752 $h^{-1}$, and revealed a better activity and selectivity for $CO_2$RR compared to formate. Lin *et al.* synthesized a CoPc and Zn–N–C (CoPc@Zn–N–C) tandem catalyst for the $CO_2$RR to form $CH_4$.[95] CoPc@Zn–N–C showed a $CH_4$/CO production rate that was over 100 times greater than that of the CoPc or Zn–N–C catalysts. Electrochemical experiments and DFT calculations revealed the two-step tandem mechanism. $CO_2$ was first reduced to CO on

CoPc, then diffused onto Zn–N–C and converted to $CH_4$. CoPc contributed to the reservoir of adsorbed *H on $ZnN_4$, which is critical to the high $CH_4$ production rate.

A change in the number of central atoms in multi-atoms site catalysts may also influence the selectivity of $C_1$ products. He *et al.* investigated the activity and selectivity of a series of multi-Fe atoms ($Fe_n$, $n$ = 1–4) doped graphdiyne catalysts for $CO_2$ electrochemical reduction using *ab initio* studies.[96] Theoretical calculations revealed $Fe_2$ and $Fe_3$ exhibited a better performance in $CO_2$-to-$CH_4$, $CO_2$-to-HCOOH, respectively. Multi-atoms site catalysts may catalyze the synthesis of $C_2^+$ products *via* multiple metal active sites. From the perspective of SACs, introducing novel metal atoms in single-atom sites also offers a novel strategy to regulate the electronic structure of the active sites.

### 2.5 Strategies to improve SAC performance

All of the aforementioned approaches have focused on improving the intrinsic nature of a single-atom site. Moreover, improving the accessibility of single-atom sites and increasing the density of single-atom sites are also promising strategies. Owing to the different synthesis strategies, there may be part of the single-atom sites that were embedded in substrates in some SACs, leading to significant loss of catalytic activities. Ye *et al.* compared the electrocatalytic performances of C-AFC©ZIF-8 and C-AFC@ZIF-8.[97] The precursor AFC©ZIF-8 was prepared by immersing ZIF-8 in ammonium ferric citrate (AFC) aqueous solution for 24 h, AFC@ZIF-8 was obtained by sealing AFC in ZIF-8. X-ray photoelectron spectroscopy (XPS) confirmed C-AFC©ZIF-8 had more Fe–N active sites on the surface than C-AFC@ZIF-8, leading to its better performance in the $CO_2$RR. Further experiments confirmed the activities of the catalysts towards the $CO_2$RR exhibited a positive correlation with the content of the exposed Fe–N active sites. Therefore, increasing the quantity of single-atom sites on the surface is viewed as an efficient way to improve the catalytic performance of SACs.

Two dimensional materials such as nanofibers constructed by one-dimension carbon materials are good choices for substrates because of their high surface areas, which can provide more space to support and anchor metal single-atom sites. Yang *et al.* reported a strategy for large-scale synthesis of a single Cu atoms catalyst supported on through-hole carbon nanofibers (CuSAs/TCNFs) for electrochemical $CO_2$-to-CO reduction.[98] Cu/ZIF-8 nanoparticles were first synthesized using the double-solvent method, and were then attached to polyacrylonitrile (PAN) nanofibers *via* the electro-spinning method (Fig. 8a). The through-hole structure offered large surface areas and improved the accessibility for Cu atom sites. At −0.9 $V_{RHE}$, CuSAs/TCNFs exhibited a maximum $FE_{MeOH}$ of 44%, and CO (56%) was obtained in the gas-phase. Later, Yang *et al.* synthesized cobalt single atoms (CoSA) supported by free-standing carbon nanofibers (HCNFs) *via* a similar strategy (Fig. 8b).[99] CoSA/HCNFs reached an extremely high current density of 211 mA $cm^{-2}$ with a 92% FE in the flow cell. MOFs with a well-defined spatial structure that can form porous carbon nanoframes through one-step pyrolysis are also viewed as a facile choice. Chen *et al.* reported SACs with Fe–$N_x$ active sites supported on mesoporous carbon nanoframes synthesized

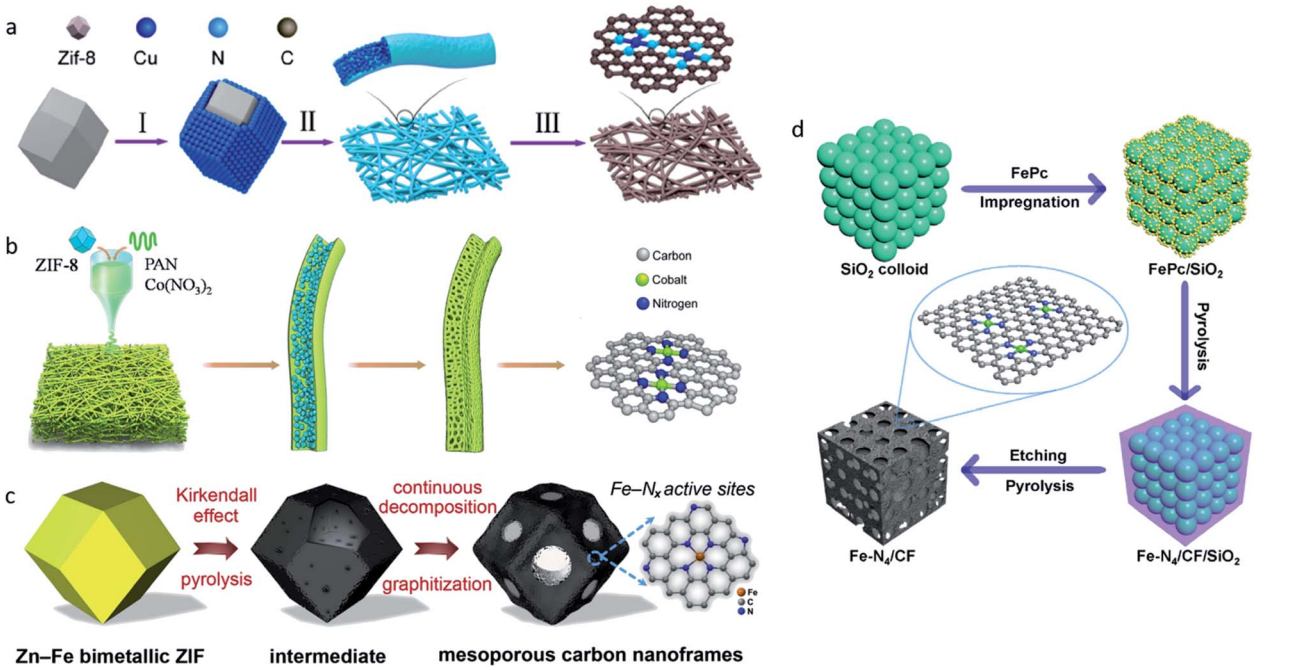


Fig. 8 (a) A schematic illustration of the synthesis of CuSAs/THCF. Reproduced from ref. 98 with permission from American Chemical Society, copyright 2019. (b) A schematic illustration of the synthesis of CoSA/HCNFs. Reproduced from ref. 99 with permission from Elsevier, copyright 2020. (c) A schematic illustration of the synthesis of FeSAs/CNF-900. Reproduced from ref. 100 with permission from Elsevier, copyright 2020. (d) A schematic illustration of the synthesis of Fe–$N_4$/CF. Reproduced from ref. 12 with permission from Springer Nature, copyright 2019.

by pyrolysis of Fe-doped MOF precursors (Fig. 8c).[100] In the pyrolysis process, spatially isolated $Fe^{2+}$ in ZIF precursors triggered the Kirkendall effect, which generated the formation of mesoporous carbon nanoframes with hierarchical pore sizes, improved the accessibility of high-density single atom Fe sites and the mass and charge transport abilities, and resulted in an extraordinary electrocatalytic performance for both oxygen and carbon dioxide reduction. The template-assisted method is also a common strategy used to synthesize high surface area substrates with the advantages of reactants and products diffusion. Zhang *et al.* proposed a template-assisted method to synthesize a Fe single-atom site catalyst confined by carbon foam (Fe–$N_4$/CF) with FePc as a precursor and $SiO_2$ as a template (Fig. 8d).[12] The pore-enriched structure boosted the diffusion of the reactants and products. Fe–$N_4$/CF reached a maximum $FE_{CO}$ of 94.9% at $-0.5$ $V_{RHE}$.

The increasing density of single-atom sites directly revealed an increase in the metal loading in SACs. The main challenge is that the aggregation tendency of the single metal atoms will increase as the distances between isolated single-atom sites become smaller owing to the increased metal contents. Chen *et al.* reported a Fe and N doped porous carbon nanosphere catalyst (Fe–N–PC) with a high Fe content of 3.9 wt%.[101] $SiO_2$ was used as the template and the protecting shell to prevent the aggregation of Fe single atoms and the volatilization of the N-containing species, leading to a high density of Fe single atoms with only a few Fe clusters. Fe–N–PC exhibited a high $FE_{CO}$ of 90% at $-0.49$ $V_{RHE}$, with a partial CO current density of 11.44 mA $cm^{-2}$. Zhao *et al.* later proposed a universal seeding strategy to synthesize a series of single metal atoms (*e.g.*, Ni, Co, Fe, Cu, Ag, Pd) and bimetallic NiCu atoms catalysts supported on 2D materials (*e.g.*, GO, $MoS_2$, BN nanosheets) with metal contents between 2.8–7.9 wt%.[102] In particular, a Ni-single-atom site catalyst supported on graphene oxide (SANi-GO) was still able to maintain an extraordinary $CO_2$RR performance after a 50 h cycling test, suggesting the excellent stability.

## 3. Outlook

The electrochemical $CO_2$RR provides a novel way to convert electricity, which can be generated from renewable energy, to chemical energy in the forms of CO, $CH_4$, and even more complicated hydrocarbon fuels. As a bridge between homogenous catalysts and heterogeneous catalysts, SACs feature single-atom sites similar to molecular catalysts with great uniformity and unique geometric and electronic structures, resulting in their outstanding performances in the $CO_2$RR.

In order to design high-performance SACs accurately, the necessity for the atomic-level regulation of SACs must be recognized. In this perspective article, the importance of the regulation of SACs at the atomic level is stressed from several aspects. The design of SACs can be divided into the regulation of SAC structures to improve the catalytic activities and selectivity. Enhancing the intrinsic nature of each single-atom site and increasing the density of the single-atom sites are the two main strategies used to improve SAC catalytic performance. The choice of the metal center and the regulation of the coordination environment are vital for the structural and electronic properties of SACs. Recently, dual- and multiple-atom sites have drawn significant attention owing to their great performance in the $CO_2$RR, especially $C_2^+$ products, and they are also important in SACs for achieving highly efficient $CO_2$RR performance. Agglomeration is a huge unavoidable hinderance to increasing the density of single-atom sites. The fine regulation of single-atom sites from both geometric and electronic angles can relieve aggregation through interactions between metal atoms and substrates. Synthetic methods also influence the performance of SACs *via* determining the accessibility of single-atom sites.

Although the development of SACs holds promise, there are still multiple challenges that must be noted:

(1) Although a large number of SACs have shown good performance for the $CO_2$RR, there is still the large potential for the improvement of the activity and selectivity, especially for $C_2^+$ products and liquid hydrocarbon fuels, which are more valuable for industrial use. Although most SACs for the $CO_2$RR catalyze $CO_2$-to-CO conversion, more effort should be made to explore C–C coupling on SACs. Also, the HER, as a common side reaction to the $CO_2$RR, should receive more attention. With appropriate regulation, the HER could work alongside the $CO_2$RR to produce syngas.[103]

(2) Although single-atom sites have great uniformity, their actual condition still remains ambiguous. An understanding of the reaction mechanism and active sites, which depends on further developments in characterization methods and the assistance of theoretical computation, is vital to the regulation of SACs at the atomic level. Advanced characterization techniques, such as *operando* characterization, are urgently needed, which can reveal the actual active sites during the catalysis reaction, thus contributing to our understanding of the mechanism, enabling the final regulation of SACs. Theoretical computation is built on known mechanisms and ideal reaction conditions; accordingly, there are differences between the results of theoretical computations and laboratory experiments. The process used to diminish the differences also offers better understanding of the reaction mechanism.

(3) It should be emphasized that there is still a long way to go for SACs to move from laboratory tests into industrial production. The scaling up of synthesis and complicated reaction conditions are the main hinderances to the practical application of SACs. Recently, several mass production methods for SACs have been reported; facile strategies or commercial reactants were used to meet industrial-scale synthesis demand.[104] However, there is a large discrepancy between the applications of SACs in half-cells and full-cells, which may be caused by transport loss and ohmic loss. In addition, SACs have to overcome the reaction conditions, which are much more unstable and impure in full-cell and industrial applications, owing to low-cost requirements.

## Conflicts of interest

There are no conflicts to declare.

## Acknowledgements

This work was supported by the National Key R&D Program of China (2018YFA0702003), the National Natural Science Foundation of China (21890383, 21671117, 21871159), Science and Technology Key Project of Guangdong Province of China (2020B010188002), Beijing Municipal Science & Technology Commission No. Z191100007219003, the National Postdoctoral Program for Innovative Talents (BX20180160), and the China Postdoctoral Science Foundation (2018M640113).

## Notes and references

1 J. D. Shakun, P. U. Clark, F. He, S. A. Marcott, A. C. Mix, Z. Liu, B. Otto-Bliesner, A. Schmittner and E. Bard, *Nature*, 2012, **484**, 49–54.
2 C. Hepburn, E. Adlen, J. Beddington, E. A. Carter, S. Fuss, N. Mac Dowell, J. C. Minx, P. Smith and C. K. Williams, *Nature*, 2019, **575**, 87–97.
3 N. Corbin, J. Zeng, K. Williams and K. Manthiram, *Nano Res.*, 2019, **12**, 2093–2125.
4 F. P. G. de Arquer, D. Cao-Thang, A. Ozden, J. Wicks, C. McCallum, A. R. Kirmani, N. Dae-Hyun, C. Gabardo, A. Seifitokaldani, X. Wang, Y. C. Li, F. Li, J. Edwards, L. J. Richter, S. J. Thorpe, D. Sinton and E. H. Sargent, *Science*, 2020, **367**, 661–666.
5 S. Lin, C. S. Diercks, Y.-B. Zhang, N. Kornienko, E. M. Nichols, Y. Zhao, A. R. Paris, D. Kim, P. Yang, O. M. Yaghi and C. J. Chang, *Science*, 2015, **349**, 1208–1213.
6 M. Liu, Y. Pang, B. Zhang, P. De Luna, O. Voznyy, J. Xu, X. Zheng, C. T. Dinh, F. Fan, C. Cao, F. P. G. de Arquer, T. S. Safaei, A. Mepham, A. Klinkova, E. Kumacheva, T. Filleter, D. Sinton, S. O. Kelley and E. H. Sargent, *Nature*, 2016, **537**, 382–386.
7 J. Graciani, K. Mudiyanselage, F. Xu, A. E. Baber, J. Evans, S. D. Senanayake, D. J. Stacchiola, P. Liu, J. Hrbek, J. Fernandez Sanz and J. A. Rodriguez, *Science*, 2014, **345**, 546–550.
8 D. Yang, B. Ni and X. Wang, *Adv. Energy Mater.*, 2020, **10**, 2001142.
9 S. Ji, Y. Qu, T. Wang, Y. Chen, G. Wang, X. Li, J. Dong, Q. Chen, W. Zhang, Z. Zhang, S. Liang, R. Yu, Y. Wang, D. Wang and Y. Li, *Angew. Chem., Int. Ed.*, 2020, **59**, 10651–10657.
10 G. Wang, C.-T. He, R. Huang, J. Mao, D. Wang and Y. Li, *J. Am. Chem. Soc.*, 2020, **142**, 19339–19345.
11 M. Li, H. Wang, W. Luo, P. C. Sherrell, J. Chen and J. Yang, *Adv. Mater.*, 2020, **32**, e2001848.
12 Z. Zhang, C. Ma, Y. Tu, R. Si, J. Wei, S. Zhang, Z. Wang, J.-F. Li, Y. Wang and D. Deng, *Nano Res.*, 2019, **12**, 2313–2317.
13 Q. Wang, Y. Lei, D. Wang and Y. Li, *Energy Environ. Sci.*, 2019, **12**, 1730–1750.
14 Y. Ouyang, L. Shi, X. Bai, Q. Li and J. Wang, *Chem. Sci.*, 2020, **11**, 1807–1813.
15 F. Li, A. Thevenon, A. Rosas-Hernandez, Z. Wang, Y. Li, C. M. Gabardo, A. Ozden, D. Cao Thang, J. Li, Y. Wang, J. P. Edwards, Y. Xu, C. McCallum, L. Tao, Z.-Q. Liang, M. Luo, X. Wang, H. Li, C. P. O'Brien, C.-S. Tan, D.-H. Nam, R. Quintero-Bermudez, T.-T. Zhuang, Y. C. Li, Z. Han, R. D. Britt, D. Sinton, T. Agapie, J. C. Peters and E. H. Sargent, *Nature*, 2020, **577**, 509–513.
16 R. Lin, X. Ma, W.-C. Cheong, C. Zhang, W. Zhu, J. Pei, K. Zhang, B. Wang, S. Liang, Y. Liu, Z. Zhuang, R. Yu, H. Xiao, J. Li, D. Wang, Q. Peng, C. Chen and Y. Li, *Nano Res.*, 2019, **12**, 2866–2871.
17 X. Li, H. Rong, J. Zhang, D. Wang and Y. Li, *Nano Res.*, 2020, **13**, 1842–1855.
18 N. Fu, X. Liang, Z. Li, W. Chen, Y. Wang, L. Zheng, Q. Zhang, C. Chen, D. Wang, Q. Peng, L. Gu and Y. Li, *Nano Res.*, 2020, **13**, 947–951.
19 B. Qiao, A. Wang, X. Yang, L. F. Allard, Z. Jiang, Y. Cui, J. Liu, J. Li and T. Zhang, *Nat. Chem.*, 2011, **3**, 634–641.
20 Z. Zhuang, Q. Kang, D. Wang and Y. Li, *Nano Res.*, 2020, **13**, 1856–1866.
21 N. Zhang, C. Ye, H. Yan, L. Li, H. He, D. Wang and Y. Li, *Nano Res.*, 2020, **13**, 3165–3182.
22 S. Ji, Y. Chen, X. Wang, Z. Zhang, D. Wang and Y. Li, *Chem. Rev.*, 2020, **120**, 11900–11955.
23 H. Rong, S. Ji, J. Zhang, D. Wang and Y. Li, *Nat. Commun.*, 2020, **11**, 5884.
24 Z. Li, Y. Chen, S. Ji, Y. Tang, W. Chen, A. Li, J. Zhao, Y. Xiong, Y. Wu, Y. Gong, T. Yao, W. Liu, L. Zheng, J. Dong, Y. Wang, Z. Zhuang, W. Xing, C.-T. He, C. Peng, W.-C. Cheong, Q. Li, M. Zhang, Z. Chen, N. Fu, X. Gao, W. Zhu, J. Wan, J. Zhang, L. Gu, S. Wei, P. Hu, J. Luo, J. Li, C. Chen, Q. Peng, X. Duan, Y. Huang, X.-M. Chen, D. Wang and Y. Li, *Nat. Chem.*, 2020, **12**, 764–772.
25 Z. Li, S. Ji, Y. Liu, X. Cao, S. Tian, Y. Chen, Z. Niu and Y. Li, *Chem. Rev.*, 2020, **120**, 623–682.
26 H. B. Yang, S.-F. Hung, S. Liu, K. Yuan, S. Miao, L. Zhang, X. Huang, H.-Y. Wang, W. Cai, R. Chen, J. Gao, X. Yang, W. Chen, Y. Huang, H. M. Chen, C. M. Li, T. Zhang and B. Liu, *Nat. Energy*, 2018, **3**, 140–147.
27 W. Zhu, L. Zhang, S. Liu, A. Li, X. Yuan, C. Hu, G. Zhang, W. Deng, K. Zang, J. Luo, Y. Zhu, M. Gu, Z.-J. Zhao and J. Gong, *Angew. Chem., Int. Ed.*, 2020, **59**, 12664–12668.
28 H. Zhang, J. Li, S. Xi, Y. Du, X. Hai, J. Wang, H. Xu, G. Wu, J. Zhang, J. Lu and J. Wang, *Angew. Chem., Int. Ed.*, 2019, **58**, 14871–14876.
29 S. Tian, M. Hu, Q. Xu, W. Gong, W. Chen, J. Yang, Y. Zhu, C. Chen, J. He, Q. Liu, H. Zhao, D. Wang and Y. Li, *Sci. China Mater.*, 2021, **64**, 642–650.
30 J. Mao, C.-T. He, J. Pei, Y. Liu, J. Li, W. Chen, D. He, D. Wang and Y. Li, *Nano Lett.*, 2020, **20**, 3442–3448.
31 X. Zhang, Z. Wu, X. Zhang, L. Li, Y. Li, H. Xu, X. Li, X. Yu, Z. Zhang, Y. Liang and H. Wang, *Nat. Commun.*, 2017, **8**, 14675.
32 K. Zhao, X. Nie, H. Wang, S. Chen, X. Quan, H. Yu, W. Choi, G. Zhang, B. Kim and J. G. Chen, *Nat. Commun.*, 2020, **11**, 2455.
33 X. Song, H. Zhang, Y. Yang, B. Zhang, M. Zuo, X. Cao, J. Sun, C. Lin, X. Li and Z. Jiang, *Adv. Sci.*, 2018, **5**, 1800177.

34 K. Jiang, S. Siahrostami, T. Zheng, Y. Hu, S. Hwang, E. Stavitski, Y. Peng, J. Dynes, M. Gangisetty, D. Su, K. Attenkofer and H. Wang, *Energy Environ. Sci.*, 2018, **11**, 893–903.

35 Y. Pan, R. Lin, Y. Chen, S. Liu, W. Zhu, X. Cao, W. Chen, K. Wu, W.-C. Cheong, Y. Wang, L. Zheng, J. Luo, Y. Lin, Y. Liu, C. Liu, J. Li, Q. Lu, X. Chen, D. Wang, Q. Peng, C. Chen and Y. Li, *J. Am. Chem. Soc.*, 2018, **140**, 4218–4221.

36 J. Zhang, C. Zheng, M. Zhang, Y. Qiu, Q. Xu, W.-C. Cheong, W. Chen, L. Zheng, L. Gu, Z. Hu, D. Wang and Y. Li, *Nano Res.*, 2020, **13**, 3082–3087.

37 X. Rong, H.-J. Wang, X.-L. Lu, R. Si and T.-B. Lu, *Angew. Chem., Int. Ed.*, 2020, **59**, 1961–1965.

38 Y.-N. Gong, L. Jiao, Y. Qian, C.-Y. Pan, L. Zheng, X. Cai, B. Liu, S.-H. Yu and H.-L. Jiang, *Angew. Chem., Int. Ed.*, 2020, **59**, 2705–2709.

39 X. Wang, Z. Chen, X. Zhao, T. Yao, W. Chen, R. You, C. Zhao, G. Wu, J. Wang, W. Huang, J. Yang, X. Hong, S. Wei, Y. Wu and Y. Li, *Angew. Chem., Int. Ed.*, 2018, **57**, 1944–1948.

40 W. Ju, A. Bagger, G. P. Hao, A. S. Varela, I. Sinev, V. Bon, B. Roldan Cuenya, S. Kaskel, J. Rossmeisl and P. Strasser, *Nat. Commun.*, 2017, **8**, 944.

41 H. Shang, W. Sun, R. Sui, J. Pei, L. Zheng, J. Dong, Z. Jiang, D. Zhou, Z. Zhuang, W. Chen, J. Zhang, D. Wang and Y. Li, *Nano Lett.*, 2020, **20**, 5443–5450.

42 T. Sun, Y. Li, T. Cui, L. Xu, Y.-G. Wang, W. Chen, P. Zhang, T. Zheng, X. Fu, S. Zhang, Z. Zhang, D. Wang and Y. Li, *Nano Lett.*, 2020, **20**, 6206–6214.

43 S. Back, J. Lim, N.-Y. Kim, Y.-H. Kim and Y. Jung, *Chem. Sci.*, 2017, **8**, 1090–1096.

44 C. Zhang, S. Yang, J. Wu, M. Liu, S. Yazdi, M. Ren, J. Sha, J. Zhong, K. Nie, A. S. Jalilov, Z. Li, H. Li, B. I. Yakobson, Q. Wu, E. Ringe, H. Xu, P. M. Ajayan and J. M. Tour, *Adv. Energy Mater.*, 2018, **8**, 1703487.

45 L. Han, S. Song, M. Liu, S. Yao, Z. Liang, H. Cheng, Z. Ren, W. Liu, R. Lin, G. Qi, X. Liu, Q. Wu, J. Luo and H. L. Xin, *J. Am. Chem. Soc.*, 2020, **142**, 12563–12567.

46 H. Shang, T. Wang, J. Pei, Z. Jiang, D. Zhou, Y. Wang, H. Li, J. Dong, Z. Zhuang, W. Chen, D. Wang, J. Zhang and Y. Li, *Angew. Chem., Int. Ed.*, 2020, **59**, 22465–22469.

47 D. Tan, J. Zhang, L. Yao, X. Tan, X. Cheng, Q. Wan, B. Han, L. Zheng and J. Zhang, *Nano Res.*, 2020, **13**, 768–774.

48 D. Gao, R. M. Aran-Ais, H. S. Jeon and B. Roldan Cuenya, *Nat. Catal.*, 2019, **2**, 198–210.

49 T. Zheng, K. Jiang and H. Wang, *Adv. Mater.*, 2018, **30**, e1802066.

50 T. Sun, L. Xu, D. Wang and Y. Li, *Nano Res.*, 2019, **12**, 2067–2080.

51 J. Yang, W. Li, D. Wang and Y. Li, *Small Struct*, 2021, **2**, 2000051.

52 Y. Chen, R. Gao, S. Ji, H. Li, K. Tang, P. Jiang, H. Hu, Z. Zhang, H. Hao, Q. Qu, X. Liang, W. Chen, J. Dong, D. Wang and Y. Li, *Angew. Chem., Int. Ed.*, 2021, **60**, 3212–3221.

53 L. Gong, D. Zhang, C.-Y. Lin, Y. Zhu, Y. Shen, J. Zhang, X. Han, L. Zhang and Z. Xia, *Adv. Energy Mater.*, 2019, **9**, 1902625.

54 Q. He, J. H. Lee, D. Liu, Y. Liu, Z. Lin, Z. Xie, S. Hwang, S. Kattel, L. Song and J. G. Chen, *Adv. Funct. Mater.*, 2020, **30**, 2000407.

55 T. Wang, Q. Zhao, Y. Fu, C. Lei, B. Yang, Z. Li, L. Lei, G. Wu and Y. Hou, *Small Methods*, 2019, **3**, 1900210.

56 J. Li, P. Prslja, T. Shinagawa, A. J. Martin Fernandez, F. Krumeich, K. Artyushkova, P. Atanassov, A. Zitolo, Y. Zhou, R. Garcia-Muelas, N. Lopez, J. Perez-Ramirez and F. Jaouen, *ACS Catal.*, 2019, **9**, 10426–10439.

57 W. Zheng, F. Chen, Q. Zeng, Z. Li, B. Yang, L. Lei, Q. Zhang, F. He, X. Wu and Y. Hou, *Nano-Micro Lett.*, 2020, **12**, 108.

58 F. Pan, H. Zhang, K. Liu, D. Cullen, K. More, M. Wang, Z. Feng, G. Wang, G. Wu and Y. Li, *ACS Catal.*, 2018, **8**, 3116–3122.

59 J. Gu, C.-S. Hsu, L. Bai, H. M. Chen and X. Hu, *Science*, 2019, **364**, 1091–1094.

60 Y. Hou, Y.-L. Liang, P.-C. Shi, Y.-B. Huang and R. Cao, *Appl. Catal., B*, 2020, **271**, 118929.

61 H.-Y. Jeong, M. Balamurugan, V. S. K. Choutipalli, E.-s. Jeong, V. Subramanian, U. Sim and K. T. Nam, *J. Mater. Chem. A*, 2019, **7**, 10651–10661.

62 W. Zhang, Y. Hu, L. Ma, G. Zhu, Y. Wang, X. Xue, R. Chen, S. Yang and Z. Jin, *Adv. Sci.*, 2018, **5**, 1700275.

63 X. Cui, W. An, X. Liu, H. Wang, Y. Men and J. Wang, *Nanoscale*, 2018, **10**, 15262–15272.

64 E. Zhang, T. Wang, K. Yu, J. Liu, W. Chen, A. Li, H. Rong, R. Lin, S. Ji, X. Zhene, Y. Wang, L. Zheng, C. Chen, D. Wang, J. Zhang and Y. Li, *J. Am. Chem. Soc.*, 2019, **141**, 16569–16573.

65 J. Yang, W. Li, D. Wang and Y. Li, *Adv. Mater.*, 2020, **32**, 2003300.

66 C. F. Wen, F. Mao, Y. Liu, X. Y. Zhang, H. Q. Fu, L. R. Zheng, P. F. Liu and H. G. Yang, *ACS Catal.*, 2020, **10**, 1086–1093.

67 S. He, D. Ji, J. Zhang, P. Novello, X. Li, Q. Zhang, X. Zhang and J. Liu, *J. Phys. Chem. B*, 2020, **124**, 511–518.

68 Q. Fan, P. Hou, C. Choi, T.-S. Wu, S. Hong, F. Li, Y.-L. Soo, P. Kang, Y. Jung and Z. Sun, *Adv. Energy Mater.*, 2020, **10**, 1903068.

69 X. Qin, S. Zhu, F. Xiao, L. Zhang and M. Shao, *ACS Energy Lett.*, 2019, **4**, 1778–1783.

70 F. Yang, P. Song, X. Liu, B. Mei, W. Xing, Z. Jiang, L. Gu and W. Xu, *Angew. Chem., Int. Ed.*, 2018, **57**, 12303–12307.

71 K. Mou, Z. Chen, X. Zhang, M. Jiao, X. Zhang, X. Ge, W. Zhang and L. Liu, *Small*, 2019, **15**, e1903668.

72 Y. Chen, Y. Yao, Y. Xia, K. Mao, G. Tang, Q. Wu, L. Yang, X. Wang, X. Sun and Z. Hu, *Nano Res.*, 2020, **13**, 2777–2783.

73 M. Kuang, A. Guan, Z. Gu, P. Han, L. Qian and G. Zheng, *Nano Res.*, 2019, **12**, 2324–2329.

74 H. Zhong, F. Meng, Q. Zhang, K. Liu and X. Zhang, *Nano Res.*, 2019, **12**, 2318–2323.

75 M. D. Hossain, Y. Huang, T. H. Yu, W. A. Goddard Iii and Z. Luo, *Nat. Commun.*, 2020, **11**, 2256.

76 Z. Geng, Y. Cao, W. Chen, X. Kong, Y. Liu, T. Yao and Y. Lin, *Appl. Catal., B*, 2019, **240**, 234–240.

77 X. Zhao and Y. Liu, *J. Am. Chem. Soc.*, 2020, **142**, 5773–5777.
78 X. Wang, Y. Pan, H. Ning, H. Wang, D. Guo, W. Wang, Z. Yang, Q. Zhao, B. Zhang, L. Zheng, J. Zhang and M. Wu, *Appl. Catal., B*, 2020, **266**, 118630.
79 H. Shen and Q. Sun, *J. Phys. Chem. C*, 2019, **123**, 29776–29782.
80 Y. Cheng, S. Zhao, H. Li, S. He, J.-P. Veder, B. Johannessen, J. Xiao, S. Lu, J. Pan, M. F. Chisholm, S.-Z. Yang, C. Liu, J. G. Chen and S. P. Jiang, *Appl. Catal., B*, 2019, **243**, 294–303.
81 J. Yang, Z. Qiu, C. Zhao, W. Wei, W. Chen, Z. Li, Y. Qu, J. Dong, J. Luo, Z. Li and Y. Wu, *Angew. Chem., Int. Ed.*, 2018, **57**, 14095–14100.
82 F. Pan, H. Zhang, Z. Liu, D. Cullen, K. Liu, K. More, G. Wu, G. Wang and Y. Li, *J. Mater. Chem. A*, 2019, **7**, 26231–26237.
83 D. M. Koshy, S. Chen, D. U. Lee, M. B. Stevens, A. M. Abdellah, S. M. Dull, G. Chen, D. Nordlund, A. Gallo, C. Hahn, D. C. Higgins, Z. Bao and T. F. Jaramillo, *Angew. Chem., Int. Ed.*, 2020, **59**, 4043–4050.
84 Z. Jiang, Y. Wang, X. Zhang, H. Zheng, X. Wang and Y. Liang, *Nano Res.*, 2019, **12**, 2330–2334.
85 J. Choi, P. Wagner, S. Gambhir, R. Jalili, D. R. MacFarlane, G. G. Wallace and D. L. Officer, *ACS Energy Lett.*, 2019, **4**, 666–672.
86 Z. Yang, X. Zhang, C. Long, S. Yan, Y. Shi, J. Han, J. Zhang, P. An, L. Chang and Z. Tang, *CrystEngComm*, 2020, **22**, 1619–1624.
87 Y. Wang, Z. Jiang, X. Zhang, Z. Niu, Q. Zhou, X. Wang, H. Li, Z. Lin, H. Zheng and Y. Liang, *ACS Appl. Mater. Interfaces*, 2020, **12**, 33795–33802.
88 H. Kim, D. Shin, W. Yang, D. H. Won, H.-S. Oh, M. W. Chung, D. Jeong, S. H. Kim, K. H. Chae, J. Y. Ryu, J. Lee, S. J. Cho, J. Seo, H. Kim and C. H. Choi, *J. Am. Chem. Soc.*, 2021, **143**, 925–933.
89 L. Lin, T. Liu, J. Xiao, H. Li, P. Wei, D. Gao, B. Nan, R. Si, G. Wang and X. Bao, *Angew. Chem., Int. Ed.*, 2020, **59**, 22408–22413.
90 A. Guan, Z. Chen, Y. Quan, C. Peng, Z. Wang, T.-K. Sham, C. Yang, Y. Ji, L. Qian, X. Xu and G. Zheng, *ACS Energy Lett.*, 2020, **5**, 1044–1053.
91 J. Jiao, R. Lin, S. Liu, W.-C. Cheong, C. Zhang, Z. Chen, Y. Pan, J. Tang, K. Wu, S.-F. Hung, H. M. Chen, L. Zheng, Q. Lu, X. Yang, B. Xu, H. Xiao, J. Li, D. Wang, Q. Peng, C. Chen and Y. Li, *Nat. Chem.*, 2019, **11**, 222–228.
92 J. Zhao, J. Zhao, F. Li and Z. Chen, *J. Phys. Chem. C*, 2018, **122**, 19712–19721.
93 W. Ren, X. Tan, W. Yang, C. Jia, S. Xu, K. Wang, S. C. Smith and C. Zhao, *Angew. Chem., Int. Ed.*, 2019, **58**, 6972–6976.
94 W. Xie, H. Li, G. Cui, J. Li, Y. Song, S. Li, X. Zhang, J. Y. Lee, M. Shao and M. Wei, *Angew. Chem., Int. Ed.*, 2020, DOI: 10.1002/anie.202014655.
95 J. Wang, X. Huang, S. Xi, H. Xu and X. Wang, *Angew. Chem., Int. Ed.*, 2020, **59**, 19162–19167.
96 T. He, L. Zhang, G. Kour and A. Du, *J. $CO_2$ Util.*, 2020, **37**, 272–277.
97 Y. F. Ye, F. Cai, H. B. Li, H. H. Wu, G. X. Wang, Y. S. Li, S. Miao, S. H. Xie, R. Si, J. Wang and X. H. Bao, *Nano Energy*, 2017, **38**, 281–289.
98 H. Yang, Y. Wu, G. Li, Q. Lin, Q. Hu, Q. Zhang, J. Liu and C. He, *J. Am. Chem. Soc.*, 2019, **141**, 12717–12723.
99 H. Yang, Q. Lin, Y. Wu, G. Li, Q. Hu, X. Chai, X. Ren, Q. Zhang, J. Liu and C. He, *Nano Energy*, 2020, **70**, 104454.
100 X. Chen, D.-D. Ma, B. Chen, K. Zhang, R. Zou, X.-T. Wu and Q.-L. Zhu, *Appl. Catal., B*, 2020, **267**, 118720.
101 Y. Chen, L. Zou, H. Liu, C. Chen, Q. Wang, M. Gu, B. Yang, Z. Zou, J. Fang and H. Yang, *J. Phys. Chem. C*, 2019, **123**, 16651–16659.
102 S. Zhao, G. Chen, G. Zhou, L.-C. Yin, J.-P. Veder, B. Johannessen, M. Saunders, S.-Z. Yang, R. De Marco, C. Liu and S. P. Jiang, *Adv. Funct. Mater.*, 2020, **30**, 1906157.
103 M. Zhang, Z. Hu, L. Gu, Q. Zhang, L. Zhang, Q. Song, W. Zhou and S. Hu, *Nano Res.*, 2020, **13**, 3206–3211.
104 L. Zhao, Y. Zhang, L.-B. Huang, X.-Z. Liu, Q.-H. Zhang, C. He, Z.-Y. Wu, L.-J. Zhang, J. Wu, W. Yang, L. Gu, J.-S. Hu and L.-J. Wan, *Nat. Commun.*, 2019, **10**, 1278.